UC Santa Cruz

UC Santa Cruz Previously Published Works

Title

Structure of interferon-stimulated gene product 15 (ISG15) from the bat species Myotis davidii and the impact of interdomain ISG15 interactions on viral protein engagement.

Permalink

https://escholarship.org/uc/item/2n93x18v

Journal

Acta Crystallographica Section D: Structural Biology, 75(Pt 1)

Authors

Langley, Caroline

Goodwin, Octavia

Dzimianski, John

et al.

Publication Date

2019

DOI

10.1107/S2059798318015322

Peer reviewed

Structure of interferon-stimulated gene product 15 (ISG15) from the bat species *Myotis davidii* and the impact of interdomain ISG15 interactions on viral protein engagement

Caroline Langley, Octavia Goodwin, John V. Dzimianski, Courtney M. Daczkowski and Scott D. Pegan*

Pharmaceutical and Biomedical Sciences, University of Georgia, 240 West Green Street, Athens, GA 30602, USA. *Correspondence e-mail: spegan@uga.edu

Bats have long been observed to be the hosts and the origin of numerous human diseases. Bats, like all mammals, rely on a number of innate immune mechanisms to combat invading pathogens, including the interferon type I, II and III responses. Ubiquitin-like interferon-stimulated gene product 15 (ISG15) is a key modulator of these interferon responses. Within these pathways, ISG15 can serve to stabilize host proteins modulating innate immune responses and act as a cytokine. Post-translational modifications of viral proteins introduced by ISG15 have also been observed to directly affect the function of numerous viral proteins. Unlike ubiquitin, which is virtually identical across all animals, comparison of ISG15s across species reveals that they are relatively divergent, with sequence identity dropping to as low as ∼58% among mammals. In addition to serving as an obstacle to the zoonotic transmission of influenza, these ISG15 species–species differences have also long been shown to have an impact on the function of viral deISGylases. Recently, the structure of the first nonhuman ISG15, originating from mouse, suggested that the structures of human ISG15 may not be reflective of other species. Here, the structure of ISG15 from the bat species *Myotis davidii* solved to 1.37 Å resolution is reported. Comparison of this ISG15 structure with those from human and mouse not only underscores the structural impact of ISG15 species–species differences, but also highlights a conserved hydrophobic motif formed between the two domains of ISG15. Using the papain-like deISGylase from Severe acute respiratory syndrome coronavirus as a probe, the biochemical importance of this motif in ISG15–protein engagements was illuminated.

1. Introduction

Interferon-stimulated gene product 15 (ISG15) has proven to be critical to the first line of defense against invading viruses: the host innate immune response. Upon viral infection, the recognition of pathogen-associated molecular patterns (PAMPs) triggers cellular signaling cascades leading to the synthesis and secretion of type I interferons (IFNs; Durfee *et al.*, 2010). The binding of these secreted IFNs to the IFN-α receptor on the surface of the original or surrounding cells activates transcription pathways leading to the synthesis of IFN-stimulated genes, including ISG15. This 15 kDa protein is composed of two ubiquitin (Ub)-like β-grasp three-dimensional folds connected by a 'hinge' (Narasimhan *et al.*, 2005). The C-terminal domain is concluded by the highly conserved LRLRGG motif, which is identical to that of Ub and is important in conjugation to cellular targets (ISGylation; Narasimhan *et al.*, 2005). Similar to ubiquitinylation, ISGylation occurs in a three-step process dependent on an E1 activating enzyme, an E2 conjugating enzyme and an E3
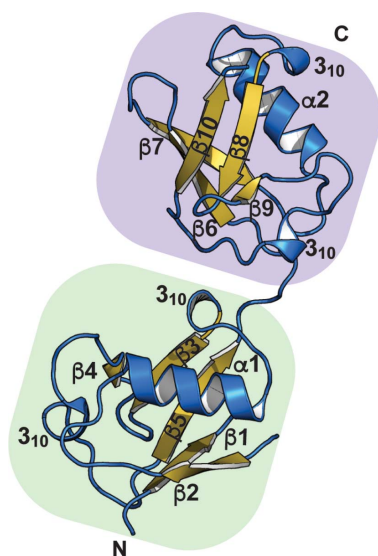
ligase. Unlike the Ub-conjugating system, which has numerous E3 enzymes associated with specific substrates, ISGylation is predominantly mediated by a single E3 enzyme (Herc5) that is responsible for the ISGylation of hundreds of proteins. As with Ube1L and UbcH8, Herc5 is induced by IFNs and physically associates with polyribosomes, leading to the co-translational ISGylation of newly synthesized proteins, including viral proteins (Dastur et al., 2006). In addition to a canonical effect through conjugation, ISG15 has also been observed to function in its unconjugated form by association with human Ub-specific protease 18 (USP18) in the regulation of IFN signaling and in an extracellular form that contributes to the induction of cytokine secretion (Speer et al., 2016; Swaim et al., 2017). Additionally, extracellular ISG15 has several immunomodulatory activities such as the induction of natural killer cell proliferation and the stimulation of IFN-γ production, triggering a type II IFN response (Bogunovic et al., 2012). ISG15 has also been linked to effective antiviral type III IFN responses (Shen et al., 2016; Murakawa et al., 2017; Fan et al., 2014).

Beyond its role as a component of these IFN responses, the importance of ISG15 has been demonstrated through knock-in studies involving a catalytically inactivated mouse USP18. Although its name would imply otherwise, USP18 is a selective deISGylase that acts to remove conjugated ISG15 from modified proteins (Kim & Zhang, 2005). Knock-in mice selectively lacking USP18 enzymatic activity exhibit enhanced and prolonged ISGylation, resulting in increased resistance against influenza, vaccinia and other viral infections (Ketscher et al., 2015; Ketscher & Knobeloch, 2015). The importance of ISG15 can also be observed through the efforts of viruses to directly engage ISG15 in attempt to downregulate immunity. Influenza B virus (IBV) encodes a nonstructural protein 1 (NS1B) that is shown to directly engage ISG15 in order to sequester ISGylated viral ribonuclear protein (RNP) to allow viral RNA synthesis (Zhao et al., 2016). Other viruses have evolved to encode their own deISGylases. In nairoviruses, a viral homologue of an ovarian tumor domain protease (vOTU) is encoded in the viral L protein along with the viral RNA polymerase (Frias-Staheli et al., 2007). Reverse genetics studies with Crimean–Congo hemorrhagic fever nairovirus revealed that a mutated vOTU lacking deISGylase activity led to lower levels of L protein, suggesting that ISG15 conjugation may destabilize it or lead to degradation (Scholte et al., 2017). Similarly, members of the coronavirus family (CoVs) include many viruses that encode deISGylases. Specifically, CoVs encode a papain-like protease PL^{pro}, or PLP2 if two papain-like proteases are encoded, that is observed to reverse ISGylation (Daczkowski, Dzimianski et al., 2017). This activity is in addition to its ability to cleave the viral polypeptide and Ub conjugates (Lindner et al., 2007).

Intriguingly, ISG15 differs from Ub in its degree of conservation among species. Ub is almost perfectly conserved among mammals, showing little variation in animals as a whole; however, the sequence identities between species for ISG15 can drop to below 60% among mammals alone (Fig. 1; Deaton et al., 2016). These differences in ISG15s between species have been shown to be a significant hindrance for NS1B from influenza to effectively engage mouse ISG15 (mISG15) on a biochemical level, impacting viral replication of influenza B in mice. As a result, ISG15 has been implicated to play a role in restricting the host range of influenza B (Sridharan et al., 2010; Versteeg et al., 2010; Yuan & Krug, 2001; Zhao et al., 2016). Recently, both nairovirus vOTUs and coronavirus PLPs have been observed to exhibit significant sensitivity to ISG15 species differences in their binding interfaces (Daczkowski, Dzimianski et al., 2017; Deaton et al., 2016). Although ISG15 has been illustrated to be physiologically important and is likely to play a role in the zoonotic potential of certain viruses, scant structural information has been available outside its human homologue. First reported in 2005, the structure of human ISG15 (hISG15) has been solved in multiple space groups, both unbound and bound to other proteins (Guan et al., 2011; James et al., 2011; Li et al., 2011; Narasimhan et al., 2005). Previously, comparison of these hISG15 structures revealed little variance at the secondary- and tertiary-structural levels despite widely different crystal packing, which appeared to support an early assumption that the observed structure of hISG15 represents a preferred conformation of ISG15s (Daczkowski, Dzimianski et al., 2017; Narasimhan et al., 2005). However, the recent elucidation of the first nonhuman ISG15 structure, that from mouse, has illustrated that the ISG15 from one species may not necessarily be representative of ISG15s as a whole.

Beyond the expected surface variations driven by primary-structural differences between the ISG15s from mice and humans, their respective Ub-like domains were twisted in substantially different orientations relative to each other (Daczkowski, Dzimianski et al., 2017). While some viral deISGylases, such as vOTUs, have only been observed to bind to the C-terminal domain of ISG15s, other viral proteins have been demonstrated to interact with both domains (Chang et al., 2008; Guan et al., 2011; Li et al., 2011; Lindner et al., 2007). Overall, this suggests that species–species differences that have an impact on ISG15–protein interactions may go beyond simple surface replacement and could include divergent interdomain interactions between ISG15 domains.

To gain greater molecular insight into the structural differences among ISG15s and how these differences have an impact on viral protease engagement, we crystallized and determined the X-ray structure of the mature full-length ISG15 from the bat *Myotis davidii*. Bat species comprise over one fifth of living mammalian species and have historically been observed to be the hosts and origin of numerous human diseases, including coronaviruses, Crimean–Congo hemorrhagic fever virus, influenza viruses and others (Kalunda et al., 1986; Li et al., 2005; Müller et al., 2016; Walker et al., 2015; Hayman, 2016; Kuchipudi & Nissly, 2018; Simmons, 2005). *M. davidii* was one of the first bat species to have the amino-acid sequence of its ISG15 made available. Apart from being a member of the large and well studied bat family *Vespertilionidae*, this vesper bat originates form the *Myotis* genus, which has over 120 members spread over six continents (Gunnell et al., 2017). As a result, its structure allows the first

insights into the structural nature of bat ISG15s. This includes structural features that are likely to be unique to vesper bat ISG15s. Additionally, the structure highlights the presence of a conserved hydrophobic patch common to ISG15s in domain–domain interactions. Given that the PL^pro from Severe acute respiratory syndrome coronavirus (SARS-CoV) engages both domains of ISG15s and has recently been shown to productively engage *M. davidii* ISG15, we use this protease as a biochemical tool; specifically, as a tool to illuminate the importance of the hydrophobic interdomain interface of ISG15 and how residue variation in this region between different species of ISG15s leads to biochemical differences in ISG15–protein engagement.

2. Materials and methods

2.1. Expression and purification of ISG15s and SARS-CoV PL^pro

The ISG15s from bat (*M. davidii*; accession No. ELK23605.1; bISG15) and human (*Homo sapiens*; accession No. AAH09507.1; hISG15) and SARS-CoV PL^pro (UniProtKB/Swiss-Prot No. P0C6U8) were cloned as described previously (Daczkowski, Dzimianski *et al.*, 2017; Deaton *et al.*, 2016). All ISG15s and SARS-CoV PL^pro were grown in 37°C in LB broth containing 100 µg ml^{-1} ampicillin. Once the optical density in these cultures reached an OD$_{600}$ of 0.6–0.8, isopropyl β-D-1-thiogalactopyranoside (IPTG) was added to a final concentration of 0.8 mM. The cells expressing SARS-CoV PL^pro were subsequently grown overnight at 25°C, whereas those expressing the ISG15s were grown overnight at 18°C. The cells were harvested by centrifugation at 5000g for 10 min and were frozen at −80°C until use.

The harvested cells expressing the ISG15s from bat and human were lysed in buffer *A* [150 mM NaCl, 50 mM HEPES pH 6.9, 10 mM imidazole, 1 mM tris(2-carboxyethyl)phosphine hydrochloride (TCEP–HCl)] and buffer *B* (500 mM NaCl, 50 mM Tris pH 8.0, 5 mg lysozyme), respectively. Once both the bat and human ISG15s had been lysed for 45 min at 4°C, they were sonicated on ice at 50% power with 5 s pulse increments for 6 min. Insoluble cell debris was removed by centrifugation at 30 000g for 30 min. The clarified supernatant was filtered with 0.80 µm nylon filters (Whatman) and flowed over high-density nickel agarose beads (Gold Biotechnology, Olivette, Missouri, USA) equilibrated with buffer *A* for bISG15 and buffer *B* for hISG15. For bISG15, the protein column was washed with buffer *A* and then eluted with buffer *A* supplemented with 300 mM imidazole. For hISG15, the protein column was washed with buffer *B* supplemented with 30 mM imidazole and then eluted with buffer *B* supplemented
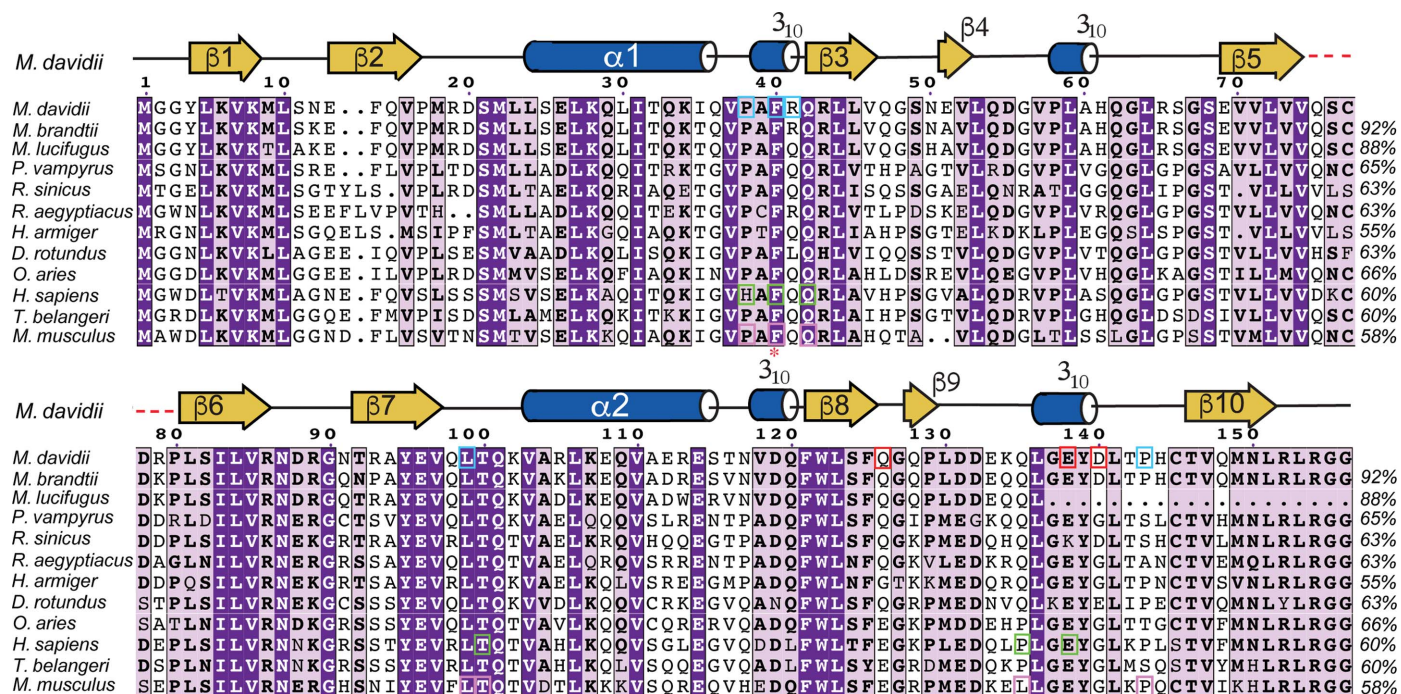

Figure 1
Sequence alignment of ISG15s from selected species. Alignment of the ISG15s from vesper bat (*M. davidii*; accession No. ELK23605.1), Brandt's bat (*M. brandtii*; accession No. XM_005871298.2), little brown bat (*M. lucifugus*; accession No. XP_014306702.1), large flying fox (*Pteropus vampyrus*; accession No. XM_011386042.2), Chinese horseshoe bat (*Rhinolophus sinicus*; accession No. XP_019567580.1), Egyptian fruit bat (*Rousettus aegyptiacus*; accession No. XP_015999857.1), great roundleaf bat (*Hipposideros armiger*; accession No. XP_019514054.1), vampire bat (*Desmodus rotundus*; accession No. XP_024410591.1), sheep (*Ovis aries*; accession No. AF152103.1), human (*H. sapiens*; accession No. AAH09507.1), northern tree shrew (*Tupaia belangeri*; accession No. AFH66859.1) and mouse (*Mus musculus*; accession No. AAB02697.1). Similarity and alignment calculations were performed using *ClustalW*. Residues involved in intradomain orientation are denoted in colored boxes (blue for bISG15, green for hISG15, pink for mISG15 and red for the negative patch in bISG15). The mutagenesis site is indicated by a red asterisk. The hinge region between the N-terminal domain and the C-terminal domain is represented by a red dashed line. The secondary-structure elements in bISG15 are shown above the alignments as predicted by *DSSP*.

with 300 mM imidazole. For use in isothermal titration calorimetry (ITC), the ISG15s were then dialyzed overnight at 4°C in buffer C [125 mM NaCl, 50 mM HEPES pH 6.9, 2 mM dithiothreitol (DTT)] with thrombin to cleave the histidine tag. They were subsequently purified by size-exclusion chromatography using a Superdex 200 column (GE Healthcare, Piscataway, New Jersey, USA). For crystallography, bISG15 was dialyzed overnight at 4°C with thrombin in buffer D (25 mM HEPES pH 6.9, 125 mM NaCl, 1 mM TCEP–HCl). The protein was loaded onto a Superdex 75 column (GE Healthcare, Pittsburgh, Pennsylvania, USA) equilibrated with buffer D.

For the purification of SARS-CoV PL^{pro}, cells expressing SARS-CoV PL^{pro} were lysed in buffer E [20 mM Tris pH 7.5, 500 mM NaCl, 10 mM β-mercaptoethanol (BME)] with 5 mg lysozyme added. After incubation for 30 min at 4°C, sonication on ice at 50% power with a 50% duty cycle was performed for a total of 6 min. Insoluble cell debris was removed by centrifugation at 70 600g for 30 min and the supernatant was filtered through 0.80 μm nylon filters (Whatman). Subsequently, the clarified supernatant was flowed over high-density nickel agarose beads (Gold Biotechnology) pre-equilibrated with buffer E. The column was washed using ten column volumes of buffer E supplemented with 30 mM imidazole. SARS-CoV PL^{pro} was eluted from the column using ten column volumes of buffer E supplemented with 300 mM imidazole. The protease was dialyzed overnight against buffer F (100 mM NaCl, 5 mM HEPES pH 7.5, 2 mM DTT) and further purified by size exclusion using a Superdex 200 column (GE Healthcare) pre-equilibrated in buffer F.

2.2. Crystallization, data processing and structure solution of bISG15

For crystallization, bISG15 was concentrated to 16 mg ml^{-1} in buffer D prior to screening against a series of NeXtal suites from Qiagen. Screening was performed in a hanging-drop format using a Mosquito robot from TTP Labtech, Hertfordshire, England. The initial screen yielded crystals in a condition consisting of 100 mM citric acid pH 4.0, 20% polyethylene glycol 6000 (PEG 6000). The crystallization conditions were optimized utilizing gradient screens and Additive Screen from Hampton Research. The final crystals were obtained by vapor diffusion using 4 μl drops equilibrated against 500 μl reservoir solution. Hanging drops were formed by mixing the protein solution in a 1:1 ratio with a precipitant solution consisting of 100 mM citric acid, 10% PEG 6000, 0.2 μl 20%(w/v) benzamidine hydrochloride.

Crystals of bISG15 were mounted on polymer loops and submerged in a cryogenic solution consisting of mother liquor with a 20% solution of 1:1:1 glycerol:dimethyl sulfoxide:polyethylene glycol (known as EDG; Sanchez et al., 2015). The crystals were then flash-cooled by submersion in liquid nitrogen. Cooled crystals were robotically mounted on a goniostat under a dry N$_2$ stream. A data set for bISG15 was collected on the SER-CAT beamline ID-22 at the Advanced Photon Source (Argonne National Laboratory, Argonne,

Table 1
Data collection and processing.

Values in parentheses are for the outer shell.

Wavelength (Å)	1.00
Temperature (K)	100
Detector	MX300-HS, Rayonix
Crystal-to-detector distance (mm)	167
Rotation range per image (°)	1.00
Total rotation range (°)	250
Exposure time per image (s)	0.5
Space group	$I2_12_12_1$
a, b, c (Å)	66.5, 68.4, 72.5
α, β, γ (°)	90.0, 90.0, 90.0
Resolution range (Å)	50–1.37 (1.39–1.37)
Total No. of reflections	730455
No. of unique reflections	34845
Completeness (%)	99.1 (96.5)
Multiplicity	9.8 (6.5)
$\langle I/\sigma(I)\rangle$	33.8 (2.92)
R_{meas}	0.058 (0.641)
Overall B factor from Wilson plot (Å^2)	19.18

Illinois, USA) using a wavelength of 1 Å and an MX300-HS detector. The data set was indexed, integrated and scaled using HKL-2000 (Otwinowski & Minor, 1997). The initial solution of the bISG15 structure was obtained by molecular replacement with Phaser (McCoy et al., 2007) utilizing a homology model derived from mouse ISG15 (PDB entry 5tla; Daczkowski, Dzimianski et al., 2017) as the search model. Once an initial solution had been obtained, it was rebuilt using AutoBuild (Adams et al., 2010). Successive rounds of manual model building and refinement were performed with Coot (Emsley et al., 2010) and PHENIX (Adams et al., 2010), respectively. Anisotropic temperature factors were used in the refinement. Water molecules were added to $F_o − F_c$ density peaks that were greater than 3σ using the 'Find Waters' function in Coot. The resulting structure was validated using MolProbity (Chen et al., 2010). Structure factors and final coordinates of the bISG15 structure have been deposited in the Protein Data Bank as entry 6mdh. Data-processing and refinement statistics are shown in Tables 1 and 2, respectively.

2.3. Site-directed mutagenesis

Mutants of bISG15 and hISG15 were generated using site-directed mutagenesis by the QuikChange approach (Agilent Technologies) according to the manufacturer's protocols. The mutant plasmids were transferred by heat-shock into Escherichia coli NEB-5α high-efficiency cells, which were then propagated and purified. The mutations were confirmed by sequencing and transferred by heat-shock into E. coli BL21(DE3) cells.

2.4. ITC of ISG15s with SARS-CoV PL^{pro}

For use in ITC, all ISG15s and SARS-CoV PL^{pro} were dialyzed overnight at 4°C in 50 mM HEPES pH 7.4, 200 mM NaCl, 1 mM DTT, 1 μM ZnCl$_2$. ZnCl$_2$ was included to maintain the stability of the PL^{pro} (Barretto et al., 2005). ITC was performed using a MicroCal PEAQ-ITC (Malvern, Worcestershire, England). 19 injections of 2 μl each at 25°C with a reference power of 5 μcal s^{-1} were collected. All results and

Table 2
Structure solution and refinement.

Values in parentheses are for the outer shell.

Resolution range (Å)	24.52–1.37 (1.40–1.37)
Completeness (%)	98.7 (95.85)
No. of reflections, working set	32946
No. of reflections, test set	1894
Final R_{cryst}	0.161
Final R_{free}	0.196
No. of non-H atoms	
Protein	1314
Water	196
Total	1510
R.m.s. deviations	
Bonds (Å)	0.014
Angles (°)	1.39
Average B factors (Å^2)	
Protein	25.39
Water	38.98
Ramachandran plot	
Most favored (%)	100
Allowed (%)	0

the associated statistics were obtained from at least two independent experiments. The SARS CoV-PL^{pro} in the cell ranged in concentration from approximately 200 to 300 µM, with a ISG15 concentration that was approximately ten times higher (∼2–3 mM) in the syringe. The data were processed using *MicroCal PEAQ-ITC Analysis Software*.

3. Results

3.1. Structure of bISG15

To obtain structural information on an ISG15 from a bat species, all 159 amino acids of the ISG15 from *M. davidii* (bISG15) were expressed with an N-terminal hexahistidine tag. Following purification by affinity and size-exclusion chromatography, bISG15 was concentrated to 16 mg ml^{-1} and screened against 768 possible commercially available crystallization conditions. Initial diamond-shaped crystals were obtained using a mixture of PEG 6000 and citric acid. Final crystal conditions were obtained using gradient and additive screening. These crystals yielded a native data set to 1.37 Å resolution in point group $I222$. Subsequently, a molecular-replacement solution for bISG15 was obtained in space group $I2_12_12_1$. The search model was derived from the recently elucidated structure of mISG15 (PDB entry 5tla; Daczkowski, Dzimianski *et al.*, 2017). Although hISG15 has a slightly higher sequence identity globally to bISG15 compared with mISG15 (60% and 58%, respectively), a recent study suggested that the interdomain interactions of ISG15s may more closely reflect those of mISG15 (Daczkowski, Dzimianski *et al.*, 2017). To generate the search model, homology models of each Ub-like β-grasp folded domain were generated using *MODELLER* (Šali & Blundell, 1993). The C-terminal domain was searched for first and then the N-terminal domain. The resulting structure of bISG15 has one bISG15 molecule in the asymmetric unit (Fig. 2a). Overall, electron density was observed for the entire mature bISG15 with the exception of the N-terminal methionine, two residues at the apex of the β1–β2

turn and the last four amino acids at the C-terminus. The lack of density for the last four amino acids mirrors previous ISG15s, where these residues have not been completely visualized outside of complexes with deISGylases (Akutsu *et al.*, 2011; Basters *et al.*, 2017; Capodagli *et al.*, 2011; Daczkowski, Dzimianski *et al.*, 2017; Daczkowski, Goodwin *et al.*, 2017; Deaton *et al.*, 2016; Guan *et al.*, 2011; James *et al.*, 2011; Li *et al.*, 2011; Narasimhan *et al.*, 2005).

Comparable to other structurally determined ISG15s, the bISG15 structure is comprised of two Ub-like β-grasp folded domains. Overall, comparing each domain of bISG15 with its counterpart in mISG15 and hISG15 reveals root-mean-square deviations (r.m.s.d.s) of 2.1 and 1.6 Å, respectively, for the N-terminal domain and 1.0 and 1.0 Å, respectively, for the C-terminal domain (Fig. 2c). Using the *Define Secondary Structure of Proteins* program (*DSSP*; Kabsch & Sander, 1983), the secondary structure of bISG15 was solved and appears to have the same ten β-strands and two α-helices as in previous ISG15 structures (Joosten *et al.*, 2011; Kabsch & Sander, 1983). However, bISG15 contains four 3$_{10}$-helices (two per domain) as in hISG15 instead of the two 3$_{10}$-helices found in mISG15 (Fig. 2a). Overall, the secondary structure of bISG15 comprises ten β-strands, two α-helices and four 3$_{10}$-helices.

Previously, an anionic ridge was observed in hISG15 but not in mISG15 (Daczkowski, Dzimianski *et al.*, 2017; Narasimhan *et al.*, 2005). To investigate whether a similar structural motif occurs in bISG15, an electrostatic potential plot of the surface of bISG15 was generated (Baker *et al.*, 2001). As in mISG15, no anionic ridge was observed on the surface of bISG15. Intriguingly, the surface of bISG15 possesses a predominantly positive surface that is more akin to that of Ub than to those of previously solved ISG15s (Fig. 2b). The one exception to this positively charged surface is a negative site formed by Gln126, Glu138 and Asp140. Whereas Glu138 is highly conserved among mammalian ISG15s, Gln126 and Asp140 show variability. In mISG15 and hISG15 these residues correspond to Glu126 and Gly140, respectively. Thus, there is an EEG site in these ISG15s compared with a QED site in bISG15. In other animals residue 126 is most commonly a glutamate or a glutamine, and in rarer cases a glycine. The most common residue found at position 140 in ISG15s is glycine, followed by the negatively charged aspartic acid and glutamic acid (Fig. 2b). The remainder is composed mostly of polar residues. Although the specific residues differ, the surface charge in this area is constantly negative in all three ISG15s, with the QED composition in bISG15 creating the most anionic patch observed among currently sequenced ISG15s. Whether this patch site has biological significance for an as yet undescribed protein–protein interaction remains a mystery. Current complexes of ISG15 with host and viral proteins do not appear to engage this region (Daczkowski, Dzimianski *et al.*, 2017; Deaton *et al.*, 2016; Narasimhan *et al.*, 2005; Basters *et al.*, 2017; Guan *et al.*, 2011). However, it does appear to be a conserved anionic patch among mammalian ISG15s and is either positioned adjacent to the interface of the Ub-like domains of the ISG15, such as in bISG15, or peripherally part of

them as in the case of other known ISG15 structures (Deaton *et al.*, 2016; Narasimhan *et al.*, 2005; Figs. 2 and 3).

3.2. Interdomain orientation differences between ISG15s

In addition to the surface differences between bISG15 and other structurally solved ISG15s, noticeable tertiary differences between these ISG15 structures were observed. When the ISG15s from bat, mouse and human sources were overlaid using a least-squares fit of the residues comprising the C-terminal domain of each structure, a noticeable difference in the twist about the C-terminal and N-terminal domains becomes apparent (Fig. 3a). Closer investigation into the interface between the domains of these three proteins reveals the potential molecular drivers for these differences (Fig. 3b). As in previous ISG15 structures, there is an apparent hydrophobic interaction between the N- and C-terminal domains of bISG15. The C-terminal side of the interaction is facilitated by Leu81, Leu99 and Pro143, with the N-terminal side principally using Phe40, which is supported in its position by Pro38. With the exception of Pro38, which is a histidine residue in hISG15, all of these positions are conserved between bISG15 and the ISG15s from mice and humans. However, just as there was a noticeable difference between the hinge regions of mISG15 and hISG15, there is also a difference in bISG15. Specifically, the hinge region of bISG15 possesses a type I reverse turn that separates bISG15 from mISG15 and hISG15. Unlike the hinge region of other ISG15s, the reverse turn directionally alters the direction of the chain, facilitating the observed bISG15 domain–domain orientation (Fig. 2 and Supplementary Fig. S1). This turn is facilitated by Ser76, Cys77, Asp78 and Arg79 (SCDR). This SCDR primary-sequence motif is NCSE in mice and KCDE in humans. With mISG15 and hISG15 lacking the serine hydroxyl group–aspartic carboxylic acid interaction, mISG15 and hISG15 are not able to replicate the tight turn that is present in bISG15. However, other mammalian ISG15s, such as that of the northern tree shrew, do have the biochemical ability to form this turn (Fig. 1). This suggests that this motif is not solely restricted to bat ISG15s but could be present in ISG15s from other species.
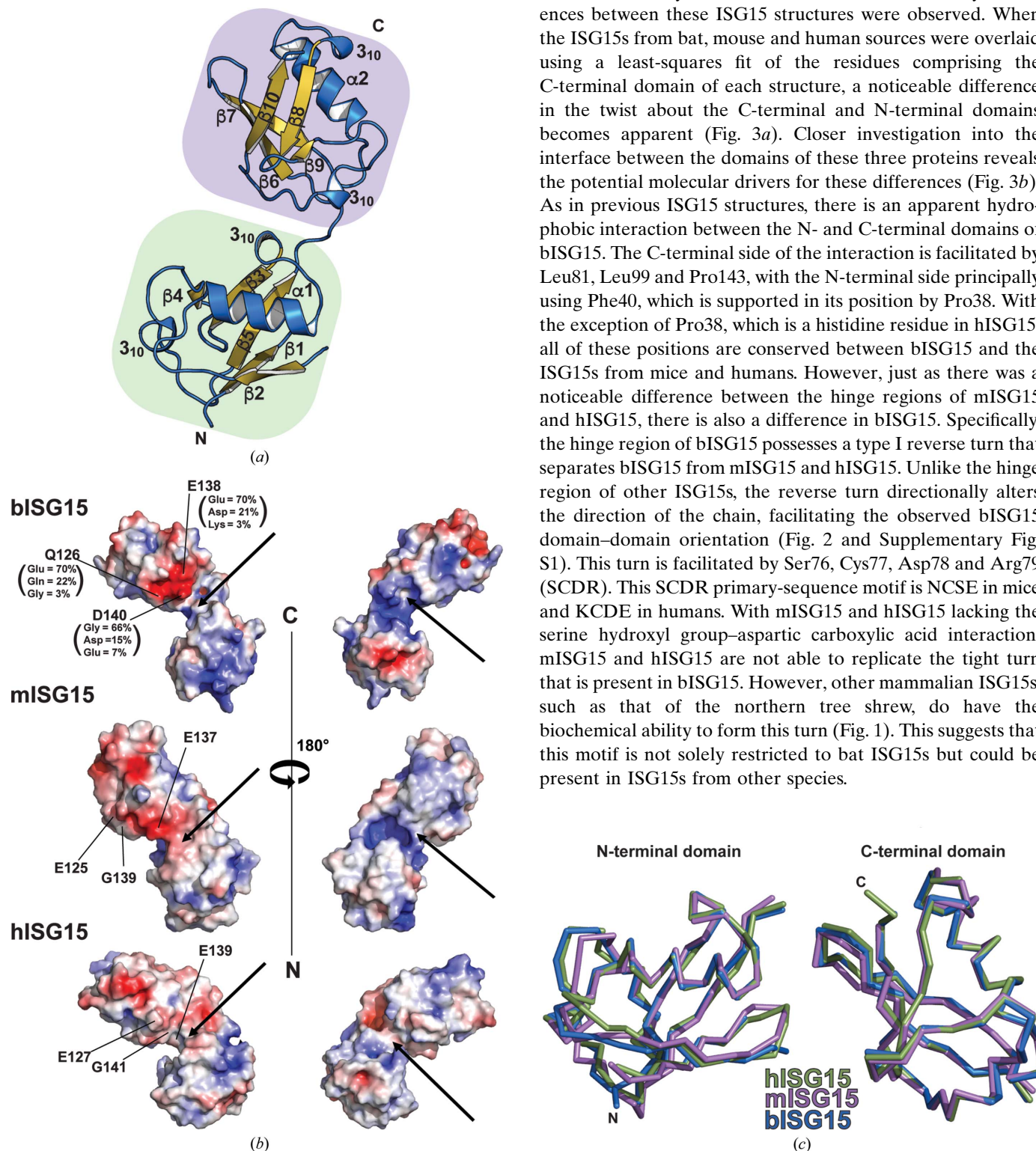

Figure 2
Structure of bISG15 shown in cartoon rendering. (*a*) The structure of the loops and helices of bISG15 is shown in blue; β-sheets are shown in gold. The N-terminus is denoted with a green background. The C-terminus is denoted with a purple background. (*b*) Electrostatic surfaces of bISG15, mISG15 and hISG15 generated using the *PDB*2*PQR* server and the surface generated using the *Adaptive Poisson–Boltzmann Solver* (*APBS*). Sequence identities for positions 126, 138 and 140 were obtained from the comparison of 92 diverse species of ISG15 and are denoted in parentheses. Arrows indicate the location of Phe40/41 buried within the interface. (*c*) The C-terminal and N-terminal domains of bISG15, hISG15 and mISG15 superimposed using the least-squares fit of residues on each respective domain.

Placing the individual domains of hISG15 and mISG15 onto the bISG15 structure does not create any steric issues for these ISG15s to adopt a bISG15 domain–domain orientation. Despite there not being any steric hindrance in this specific conformation, it is questionable whether hISG15 would be able to adopt it. Specifically, hISG15 contains a nonconserved histidine, His39, that has been suggested to stabilize its conformation. Furthermore, this histidine presents a steric hindrance to hISG15 adopting a conformation similar to that observed for mISG15, which would likely be an intermediate that hISG15 would have to pass through in order to attain the bISG15 interdomain arrangement (Daczkowski, Dzimianski *et al.*, 2017). Taking into account that the hISG15 structure is almost entirely unchanged between free and protein-bound structures with different crystal packing only underscores that it is unlikely to adopt the bISG15 conformation (Daczkowski, Dzimianski *et al.*, 2017). On the contrary, mISG15 has been observed to have a higher degree of flexibility in its domain–domain arrangements, suggesting that the barriers for mISG15 to adopt the bISG15 confirmation may be lower (Basters *et al.*, 2017; Daczkowski, Dzimianski *et al.*, 2017). However, the lack of the stabilizing reverse-turn motif in mISG15 would suggest that this conformation may not be as energetically stable for mISG15 as it is for bISG15. Naturally, this does not mean that bISG15 could not adopt a different orientation upon forming protein–protein interactions, just that it may spend more time in the currently observed domain–domain orientation.

3.3. Influence of interdomain interactions on ISG15–viral protein binding

The reoccurring presence of a hydrophobic patch centered around a conserved phenylalanine residue among the structurally determined ISG15s appears to suggest that this type of domain–domain interaction is typical for ISG15s. This furthers the assertion that the two domains of ISG15 may not operate as beads on a string, but form a domain–domain interface that is favorable for the formation of protein–protein interactions. Whereas some viral proteins, such as viral ovarian tumor domain proteases (vOTUs), have been shown to interact with solely the C-terminal domain of ISG15s (Deaton *et al.*, 2014; James *et al.*, 2011), other viral proteins have been observed to engage additional regions of ISG15. These include, for example, coronavirus proteases and host ISGylation proteins, as well as nonstructural protein 1B from influenza B (Chang *et al.*, 2008; Daczkowski, Dzimianski *et al.*, 2017; Guan *et al.*, 2011; Li *et al.*, 2011; Lindner *et al.*, 2007). To provide a better
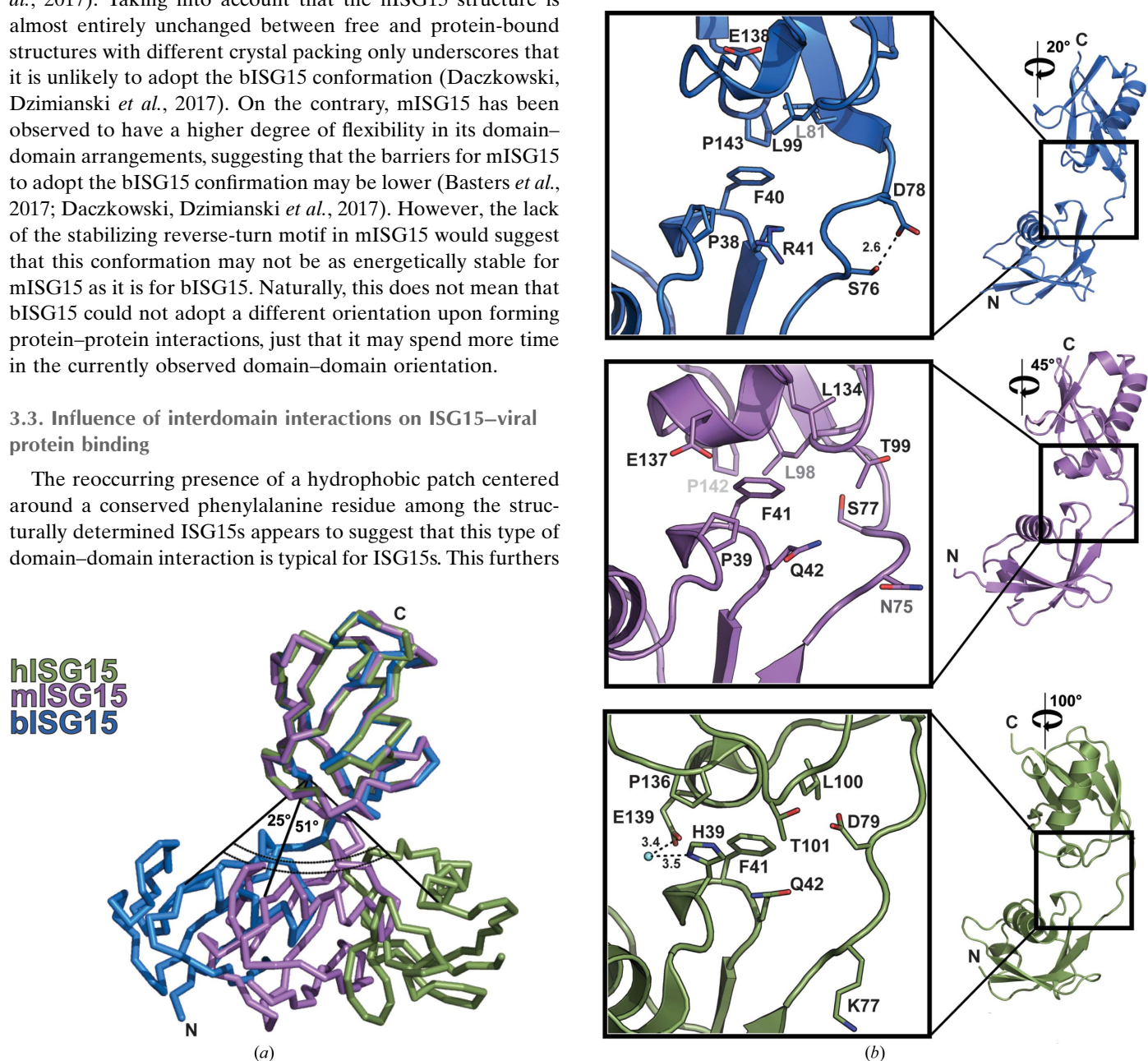

Figure 3
Overlay of ISG15s from bat, mouse and human. (*a*) The structures of hISG15 (green), mISG15 (purple) and bISG15 (blue) are superimposed using the least-squares fit of residues comprising the C-terminal domain of the respective proteins. (*b*) Close-up views of the hinge region of ISG15s from bat, mouse and human. The labeled angles indicate the rotations of each molecule relative to the orientation shown in (*a*). Dashed lines represent hydrogen bonds; distances are shown in ångströms.

Table 3
Affinity studies for SARS-CoV PL^{pro}.

	N†	K_d (μM)	ΔH‡ (kJ mol⁻¹)	ΔG§ (kJ mol⁻¹)	$-T\Delta S$¶ (kJ mol⁻¹)
bISG15	0.73 ± 0.02	29.7 ± 6.7	−21.6 ± 1.4	−25.9	−4.2
bISG15 F40A	0.75 ± 0.01	124 ± 11.3	−26.8 ± 1.4	−22.3	4.5
bISG15 F40Q	0.81 ± 0.02	127 ± 20.3	−26.1 ± 2.3	−22.3	3.8
bISG15 F40K	0.82 ± 0.06	167 ± 24.6	−32.8 ± 3.2	−21.6	11.2
hISG15††	0.93 ± 0.03	20.5 ± 4.5	−27.2 ± 1.9	−26.8	0.38
hISG15 F41A	1.09 ± 0.01	113 ± 17.1	−30.2 ± 2.4	−22.5	7.7
hISG15 F41Q	0.79 ± 0.11	152 ± 57.7	−45.0 ± 15.8	−21.9	23.2
hISG15 F41K		>50 000			
hISG15 H39P	0.76 ± 0.02	63.2 ± 10.0	−20.8 ± 1.5	−24.0	−9.8

† Binding stoichiometry.   ‡ Binding enthalpy.   § Gibb's free energy.   ¶ Entropy factor.   †† Data taken from Daczkowski *et al.* (2017).

context as to whether there is a need for ISG15 domains to interact for productive protein–protein interactions, isothermal titration calorimetry (ITC) was employed using SARS-CoV PL^{pro} as a probe. SARS-CoV PL^{pro} was selected as a probe owing to its proven biochemical ability to engage with both domains of ISG15s as well as with the ISG15 from *M. davidii* (Daczkowski, Dzimianski *et al.*, 2017; Lindner *et al.*, 2007). Although the endogenous region of *M. davidii* overlaps

with the original SARS-CoV outbreak, this species of bat was not individually investigated as a host for SARS-CoV. However, bats of the *Myotis* genus have been observed to be hosts for other coronaviruses (Liu *et al.*, 2005; Subudhi *et al.*, 2017; Tang *et al.*, 2006). In addition, receptor angiotensin-converting enzyme 2 (ACE2) from *M. daubentonii* is able to interact with the SARS-CoV spike protein, suggesting that bats in the *Myotis* genus could be susceptible to SARS-CoV infection (Hou *et al.*, 2010).

To gain information on whether the domain–domain interactions were important for ISG15–protein interactions, the affinity of SARS-CoV PL^{pro} for bISG15 was compared with the affinity of SARS-CoV PL^{pro} for various bISG15s containing mutations at the Phe40 site (Table 3, Fig. 4). Beyond being highly conserved and at the center of what structurally appears to be a hydrophobic interdomain interaction, Phe40 falls well outside the proposed SARS-CoV PL^{pro} interface (Daczkowski, Dzimianski *et al.*, 2017). As a result, modification of this site would not directly impact the SARS-CoV PL^{pro} interface but only the ability of the ISG15 domains to interact and present the proposed interface to the protease (Fig. 4). The dissociation constant (K_d) for bISG15
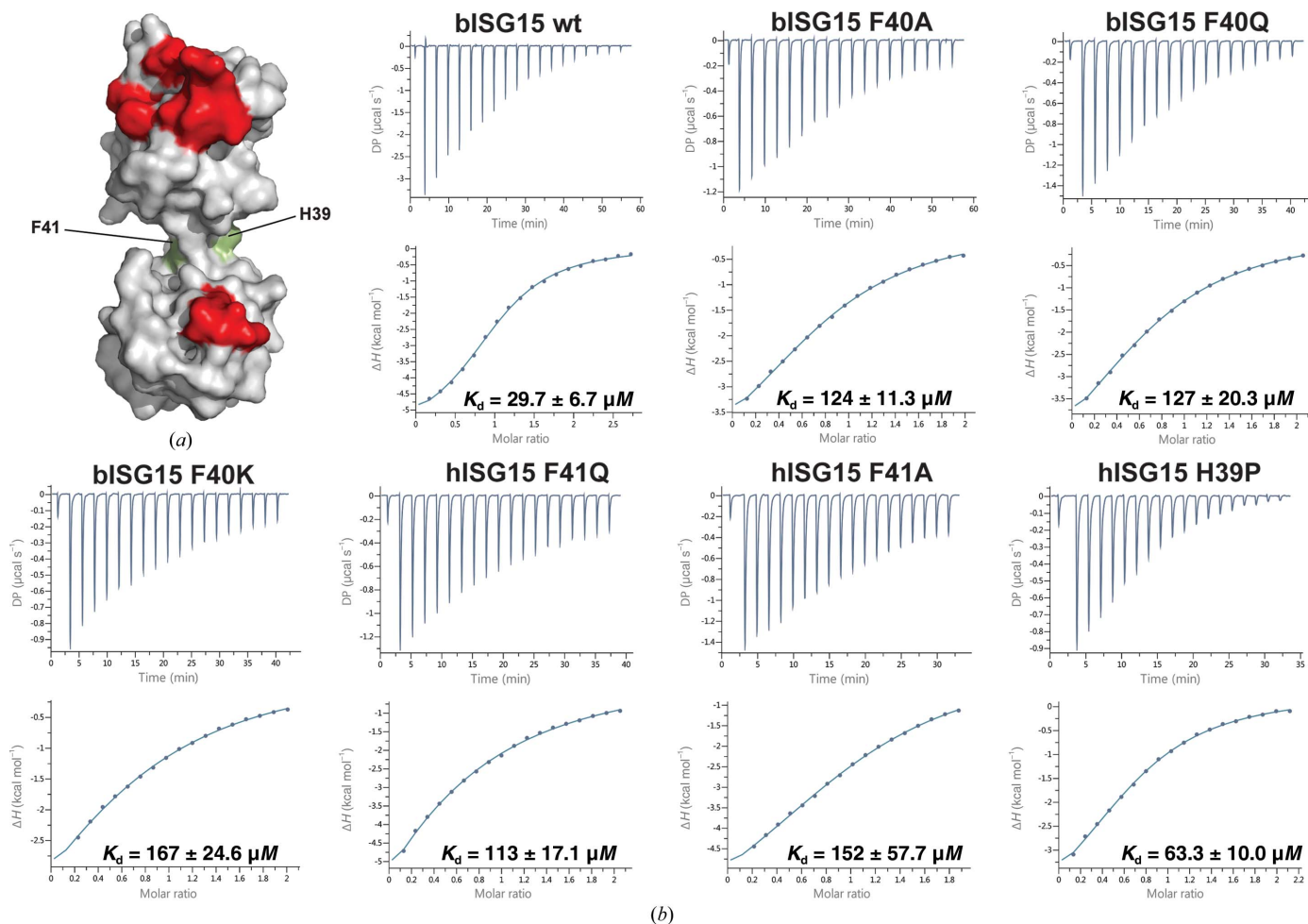

Figure 4
ITC binding isotherms for ISG15s and SARS-CoV PL^{pro}. (*a*) hISG15 with its predicted binding-interface residues with SARS-CoV PL^{pro} colored red and the sites of Phe41 and His39 colored green. (*b*) Top, representative ITC binding isotherms with the raw heats. Bottom, representative integrated heat peak areas against the molar ratio of ISG15 added to SARS-CoV PL^{pro}. The line shows the best fit to an independent model.

and the SARS-CoV PL^pro was found to be 29.7 ± 6.68 μM. Although this K_d was comparable with previously reported values for hISG15–SARS-CoV PL^pro interactions (Daczkowski, Dzimianski et al., 2017), the thermodynamic make-up of the binding event was divergent entropically. Specifically, global bISG15–SARS-CoV PL^pro interactions for both bISG15 and hISG15 were favored enthalpically. In contrast to the interactions for hISG15–SARS-CoV PL^pro interactions being marginally entropically unfavorable, those for bISG15–SARS-CoV PL^pro were entropically favorable.

The introduction of an alanine mutation at position 40 resulted in a K_d of 124 ± 11.3 μM, which was an approximately fivefold decrease in affinity. Replacing Phe40 with glutamine had a similar effect, resulting in a K_d of 127 ± 20.3 μM. The reduction in affinity between SARS-CoV PL^pro and bISG15 containing lysine at position 40 was slightly greater than for the other two mutants, with a K_d of 167 ± 24.6 μM. Interactions between comparably mutated hISG15s and SARS-CoV PL^pro followed the same disruptive trend (Table 3, Fig. 4). The introduction of the alanine mutation and the glutamine mutation resulted in appreciably reduced K_d values of 113 ± 17.1 and 152 ± 57.7 μM, respectively. These were approximately fivefold and sixfold deviations from the previously reported K_d of hISG15 for SARS-CoV PL^pro of 20.50 ± 4.48 μM (Daczkowski, Dzimianski et al., 2017). As with the bISG15–SARS-CoV PL^pro interactions, the lysine mutation in hISG15 equivalent to position 40 in bISG15 led to the most striking decrease in affinity. However, the decrease was more pronounced in hISG15, resulting in the K_d being too large to determine and suggesting that the hISG15 interdomain interface was less amenable to either the charge or the larger size of the lysine side chain than that in bISG15 when trying to adopt an attractive domain–domain binding conformation with which the protease could engage.

In addition to the similar trend of decreasing affinity from the introduction of these mutations into the ISG15s from bat and human, an interesting trend among the thermodynamic components driving these protease–ISG15 binding events was also observed. All of the mutations incurred a substantial entropic penalty. For some of the mutants in which a phenylalanine was replaced by a charged residue, an increase in the favorable enthalpic component partially offset this increase in unfavorable entropy-related events. This may suggest that these charged mutations may be able to form some favorable electrostatic interactions to make up the entropic cost that they incur. When phenylalanine was replaced by alanine within the two ISG15s, only an entropic penalty was observed in relation to the ISG15–SARS-CoV PL^pro binding events. Although ITC measures entropic and enthalpic components in aggregate, the incurrence of an entropic penalty for the mutants without an enthalpic penalty would be consistent with SARS-CoV PL^pro engaging a substrate where the electrostatics are the same but that has more degrees of freedom; in other words, going from a system in which the protease is engaging an ISG15 where the orientations of its two domains are somewhat internally restrained to one in which they are not.

Beyond the Phe40 position, His39 was also investigated for its contribution to a favorable hISG15–SARS-CoV PL^pro interaction. Previously, a report highlighted His39 as playing a role in the stability of the domain–domain orientation of hISG15, which is consistently observed over multiple structures of hISG15 alone and in complex with other proteins (Guan et al., 2011; Li et al., 2011; Narasimhan et al., 2005; James et al., 2011). Within these structures, His39 forms a hydrogen-bond network with Glu139. Whereas the glutamate is well conserved among ISG15s, histidine at position 39 is a rarity. The equivalent position in ISG15s from other species is occupied by a proline. To probe the importance of the presence of histidine over proline at this position, the affinity of hISG15 carrying a H39P mutation for SARS-CoV PL^pro was obtained. Interestingly, this mutation resulted in a threefold difference in K_d (63.2 ± 9.95 μM). To put this in perspective, this affinity mirrors that of the interaction between SARS-CoV PL^pro and solely the C-terminal domain of hISG15 (Daczkowski, Dzimianski et al., 2017). Taking the ITC data as a whole, the impact of mutations at Phe40 in bISG15 and its counterparts highlights the importance of ISG15 interdomain interactions in the effective binding of ISG15 by a protein that engages more than one domain of ISG15. Also, the impact of the H39P mutation may suggest that interdomain interactions could stabilize one orientation of the two ISG15 domains that are sliding across a hydrophobic interface and support more efficient ISG15–protein interactions.

3.4. Diversity among ISG15s originating from the order Chiroptera

Given the species–species structural differences highlighted by recently structurally determined ISG15s from nonhuman species and that the sequence identity among bat species can dip to as low as ~60%, the potential impact of this intra-family sequence diversity on the structure of ISG15 was examined. To this end, a ConSurf surface rendering (Fig. 5) was generated using all currently known complete ISG15 sequences from bats and the two sequences from the genus Myotis (Ashkenazy et al., 2016). Not surprisingly, the hydrophobic interface between the two domains of ISG15 was the most conserved. However, the reverse-turn motif found in M. davidii and other mammals appears to be limited to the Myotis genus within known bat ISG15 sequences. Even a partial ISG15 sequence from M. lucifugus (accession No. XP_014306702) possesses this motif. As a result, other bat ISG15s may behave differently in relation to their domain–domain orientation flexibility. Proteins such as influenza NS1B that engage this region may also be impacted by these differences. Beyond the disparities noted in the hinge region among bat species, the most variable areas of the sequence observed between all species of bat were also the most variable between bats from the Myotis genus. These areas of variability appear to occur in two bands, one per domain, located as the residues continue outwards towards the termini from the hinge region. Certain residues in the C-terminal band

of variability, Pro129, Leu130 and Asp132, have previously been implicated in facilitating the interactions of ISG15 with nairovirus vOTUs (Akutsu *et al.*, 2011; Capodagli *et al.*, 2011, 2013; Deaton *et al.*, 2016; James *et al.*, 2011). Additionally, the positions equivalent to those of Gln148, Asp132 and Asp88 in bISG15 have been observed to form key interactions with coronavirus PL^pro^s (Daczkowski, Goodwin *et al.*, 2017; Daczkowski, Dzimianski *et al.*, 2017). These residues are perfectly conserved within the *Myotis* genus, suggesting that the impact

of species–species differences within ISG15s is likely to be limited at the genus level. There is less information available for the N-terminal domain on the identity of residues that participate in protein–protein interactions. However, the variable region in this domain when comparing all known full-length sequences of bat ISG15s encompasses residues 12–20 and 46–50. As for ISG15s overall, the N-terminal domain shows more variability between species of bat than the C-terminal domain. However, within the *Myotis* genus the N-terminal domain is actually more conserved than its C-terminal counterpart. In fact, of the 12 residues that are not perfectly conserved between *M. davidii* and *M. brandtii*, only four are located in the N-terminal domain. Put together, the structures of ISG15s originating from species within the same genus are highly likely to be conserved, but this may not be the case at the family level and beyond.

4. Conclusion

Here, the structure of the ISG15 from the bat species *M. davidii* is reported. Through comparison of this structure with those of ISG15s from humans and mice, the presence of a reverse type I turn motif in the ISG15s from some species was revealed. Additionally, the bISG15 structure highlights an anionic patch that is conserved in mammals and reinforces the assertion of a biochemically relevant hydrophobic interface between the two Ub-like β-grasp folded domains in ISG15. Mutational analysis of this interface demonstrates that not only do ISG15 interdomain interactions play an important role in binding events between ISG15 and other proteins, but that species–species variations within this domain can also impact these events.

Figure 5
Surface features of bat ISG15s. *ConSurf* surface rendering of conserved residues in all available bat ISG15s (those from *M. davidii*, *M. brandtii*, *D. rotundus*, *P. vampyrus*, *R. sinicus*, *H. armiger* and *R. aegyptiacus*; left) and in available *Myotis* bat sequences (*M. davidii* and *M. brandtii*; right) using *M. davidii* as the reference structure. *M. lucifugus* was not included owing to only a partial sequence being available; however, the available sequence is 88.24% conserved when compared with that of *M. davidii*.

References

Adams, P. D., Afonine, P. V., Bunkóczi, G., Chen, V. B., Davis, I. W., Echols, N., Headd, J. J., Hung, L.-W., Kapral, G. J., Grosse-Kunstleve, R. W., McCoy, A. J., Moriarty, N. W., Oeffner, R., Read, R. J., Richardson, D. C., Richardson, J. S., Terwilliger, T. C. & Zwart, P. H. (2010). *Acta Cryst.* D**66**, 213–221.
Akutsu, M., Ye, Y., Virdee, S., Chin, J. W. & Komander, D. (2011). *Proc. Natl Acad. Sci. USA*, **108**, 2228–2233.
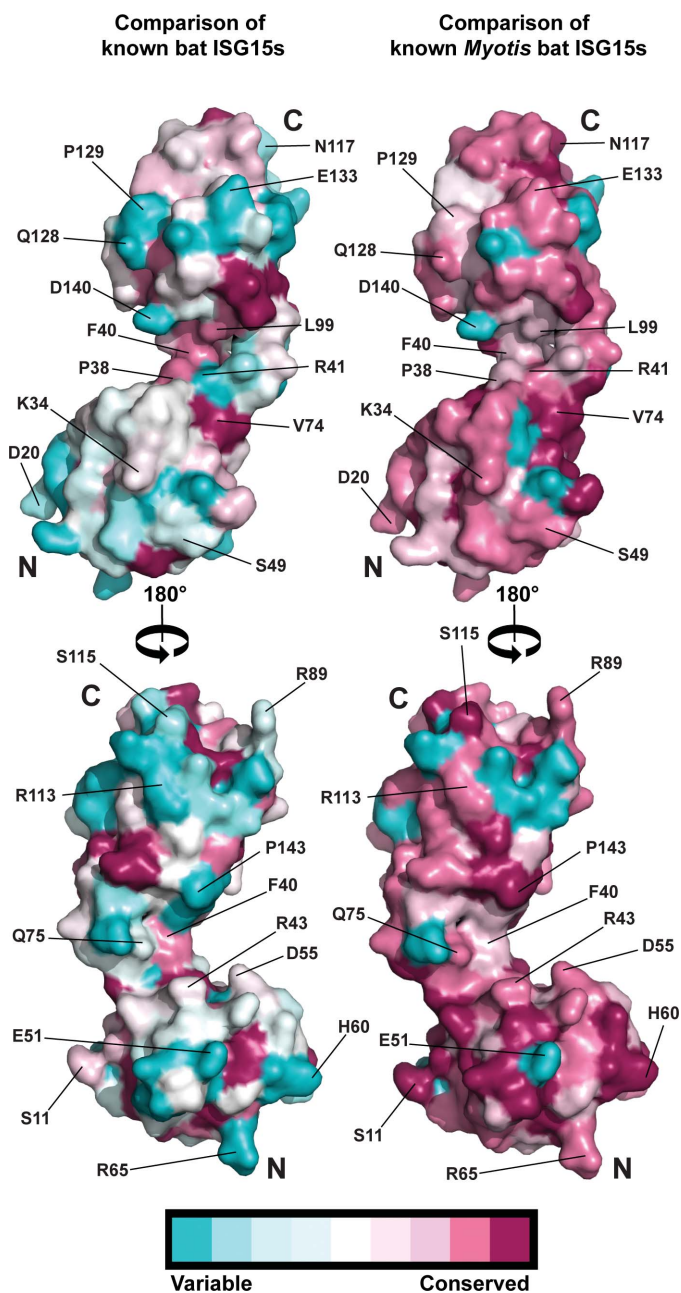
Ashkenazy, H., Abadi, S., Martz, E., Chay, O., Mayrose, I., Pupko, T. & Ben-Tal, N. (2016). *Nucleic Acids Res.* **44**, W344–W350.

Baker, N. A., Sept, D., Joseph, S., Holst, M. J. & McCammon, J. A. (2001). *Proc. Natl Acad. Sci. USA*, **98**, 10037–10041.

Barretto, N., Jukneliene, D., Ratia, K., Chen, Z., Mesecar, A. D. & Baker, S. C. (2005). *J. Virol.* **79**, 15189–15198.

Basters, A., Geurink, P. P., Röcker, A., Witting, K. F., Tadayon, R., Hess, S., Semrau, M. S., Storici, P., Ovaa, H., Knobeloch, K.-P. & Fritz, G. (2017). *Nature Struct. Mol. Biol.* **24**, 270–278.

Bogunovic, D., Byun, M., Durfee, L. A., Abhyankar, A., Sanal, O., Mansouri, D., Salem, S., Radovanovic, I., Grant, A. V., Adimi, P., Mansouri, N., Okada, S., Bryant, V. L., Kong, X.-F., Kreins, A., Velez, M. M., Boisson, B., Khalilzadeh, S., Ozcelik, U., Darazam, I. A., Schoggins, J. W., Rice, C. M., Al-Muhsen, S., Behr, M., Vogt, G., Puel, A., Bustamante, J., Gros, P., Huibregtse, J. M., Abel, L., Boisson-Dupuis, S. & Casanova, J.-L. (2012). *Science*, **337**, 1684–1688.

Capodagli, G. C., Deaton, M. K., Baker, E. A., Lumpkin, R. J. & Pegan, S. D. (2013). *J. Virol.* **87**, 3815–3827.

Capodagli, G. C., McKercher, M. A., Baker, E. A., Masters, E. M., Brunzelle, J. S. & Pegan, S. D. (2011). *J. Virol.* **85**, 3621–3630.

Chang, Y.-G., Yan, X.-Z., Xie, Y.-Y., Gao, X.-C., Song, A.-X., Zhang, D.-E. & Hu, H.-Y. (2008). *J. Biol. Chem.* **283**, 13370–13377.

Chen, V. B., Arendall, W. B., Headd, J. J., Keedy, D. A., Immormino, R. M., Kapral, G. J., Murray, L. W., Richardson, J. S. & Richardson, D. C. (2010). *Acta Cryst.* D**66**, 12–21.

Daczkowski, C. M., Dzimianski, J. V., Clasman, J. R., Goodwin, O., Mesecar, A. D. & Pegan, S. D. (2017). *J. Mol. Biol.* **429**, 1661–1683.

Daczkowski, C. M., Goodwin, O., Dzimianski, J. V., Farhat, J. J. & Pegan, S. D. (2017). *J. Virol.* **91**, e01067-17.

Dastur, A., Beaudenon, S., Kelley, M., Krug, R. M. & Huibregtse, J. M. (2006). *J. Biol. Chem.* **281**, 4334–4338.

Deaton, M. K., Dzimianski, J. V., Daczkowski, C. M., Whitney, G. K., Mank, N. J., Parham, M. M., Bergeron, E. & Pegan, S. D. (2016). *J. Virol.* **90**, 8314–8327.

Deaton, M. K., Spear, A., Faaberg, K. S. & Pegan, S. D. (2014). *Virology*, **454–455**, 247–253.

Durfee, L. A., Lyon, N., Seo, K. & Huibregtse, J. M. (2010). *Mol. Cell*, **38**, 722–732.

Emsley, P., Lohkamp, B., Scott, W. G. & Cowtan, K. (2010). *Acta Cryst.* D**66**, 486–501.

Fan, W., Xu, L., Ren, L., Qu, H., Li, J., Liang, J., Liu, W., Yang, L. & Luo, T. (2014). *J. Interferon Cytokine Res.* **34**, 848–857.

Frias-Staheli, N., Giannakopoulos, N. V., Kikkert, M., Taylor, S. L., Bridgen, A., Paragas, J. J., Richt, J. A., Rowland, R. R., Schmaljohn, C. S., Lenschow, D. J., Snijder, E. J., García-Sastre, A. & Virgin, H. W. IV (2007). *Cell Host Microbe*, **2**, 404–416.

Guan, R., Ma, L.-C., Leonard, P. G., Amer, B. R., Sridharan, H., Zhao, C., Krug, R. M. & Montelione, G. T. (2011). *Proc. Natl Acad. Sci. USA*, **108**, 13468–13473.

Gunnell, G. F., Smith, R. & Smith, T. (2017). *PLoS One*, **12**, e0172621.

Hayman, D. T. (2016). *Annu. Rev. Virol.* **3**, 77–99.

Hou, Y., Peng, C., Yu, M., Li, Y., Han, Z., Li, F., Wang, L.-F. & Shi, Z. (2010). *Arch. Virol.* **155**, 1563–1569.

James, T. W., Frias-Staheli, N., Bacik, J.-P., Levingston Macleod, J. M., Khajehpour, M., García-Sastre, A. & Mark, B. L. (2011). *Proc. Natl Acad. Sci. USA*, **108**, 2222–2227.

Joosten, R. P., te Beek, T. A. H., Krieger, E., Hekkelman, M. L., Hooft, R. W. W., Schneider, R., Sander, C. & Vriend, G. (2011). *Nucleic Acids Res.* **39**, D411–D419.

Kabsch, W. & Sander, C. (1983). *Biopolymers*, **22**, 2577–2637.

Kalunda, M., Mukwaya, L. G., Mukuye, A., Lule, M., Sekyalo, E., Wright, J. & Casals, J. (1986). *Am. J. Trop. Med. Hyg.* **35**, 387–392.

Ketscher, L., Hannss, R., Morales, D. J., Basters, A., Guerra, S., Goldmann, T., Hausmann, A., Prinz, M., Naumann, R., Pekosz, A., Utermöhlen, O., Lenschow, D. J. & Knobeloch, K.-P. (2015). *Proc. Natl Acad. Sci. USA*, **112**, 1577–1582.

Ketscher, L. & Knobeloch, K.-P. (2015). *Cytokine*, **76**, 569–571.

Kim, K. I. & Zhang, D.-E. (2005). *Methods Enzymol.* **398**, 491–499.

Kuchipudi, S. V. & Nissly, R. H. (2018). *Vet. Sci.* **5**, 71.

Li, L., Wang, D., Jiang, Y., Sun, J., Zhang, S., Chen, Y. & Wang, X. (2011). *J. Biol. Chem.* **286**, 30258–30262.

Li, W., Shi, Z., Yu, M., Ren, W., Smith, C., Epstein, J. H., Wang, H., Crameri, G., Hu, Z., Zhang, H., Zhang, J., McEachern, J., Field, H., Daszak, P., Eaton, B. T., Zhang, S. & Wang, L.-F. (2005). *Science*, **310**, 676–679.

Lindner, H. A., Lytvyn, V., Qi, H., Lachance, P., Ziomek, E. & Ménard, R. (2007). *Arch. Biochem. Biophys.* **466**, 8–14.

Liu, W., Tang, F., Fontanet, A., Zhan, L., Wang, T.-B., Zhang, P.-H., Luan, Y.-H., Cao, C.-Y., Zhao, Q.-M., Wu, X.-M., Xin, Z.-T., Zuo, S.-Q., Baril, L., Vabret, A., Shao, Y.-M., Yang, H. & Cao, W.-C. (2005). *Emerg. Infect. Dis.* **11**, 1420–1424.

McCoy, A. J., Grosse-Kunstleve, R. W., Adams, P. D., Winn, M. D., Storoni, L. C. & Read, R. J. (2007). *J. Appl. Cryst.* **40**, 658–674.

Müller, M. A., Devignot, S., Lattwein, E., Corman, V. M., Maganga, G. D., Gloza-Rausch, F., Binger, T., Vallo, P., Emmerich, P., Cottontail, V. M., Tschapka, M., Oppong, S., Drexler, J. F., Weber, F., Leroy, E. M. & Drosten, C. (2016). *Sci. Rep.* **6**, 26637.

Murakawa, M., Asahina, Y., Kawai-Kitahata, F., Nakagawa, M., Nitta, S., Otani, S., Nagata, H., Kaneko, S., Asano, Y., Tsunoda, T., Miyoshi, M., Itsui, Y., Azuma, S., Kakinuma, S., Tanaka, Y., Iijima, S., Tsuchiya, K., Izumi, N., Tohda, S. & Watanabe, M. (2017). *J. Med. Virol.* **89**, 1241–1247.

Narasimhan, J., Wang, M., Fu, Z., Klein, J. M., Haas, A. L. & Kim, J.-J. P. (2005). *J. Biol. Chem.* **280**, 27356–27365.

Otwinowski, Z. & Minor, W. (1997). *Methods Enzymol.* **276**, 307–326.

Sanchez, J. E., Gross, P. G., Goetze, R. W., Walsh, R. M., Peeples, W. B. & Wood, Z. A. (2015). *Biochemistry*, **54**, 3360–3369.

Šali, A. & Blundell, T. L. (1993). *J. Mol. Biol.* **234**, 779–815.

Scholte, F. E. M., Zivcec, M., Dzimianski, J. V., Deaton, M. K., Spengler, J. R., Welch, S. R., Nichol, S. T., Pegan, S. D., Spiropoulou, C. F. & Bergeron, E. (2017). *Cell. Rep.* **20**, 2396–2407.

Shen, H., Zhang, C., Guo, P., Liu, Z., Sun, M., Sun, J., Li, L., Dong, J. & Zhang, J. (2016). *Virus Genes*, **52**, 877–882.

Simmons, N. B. (2005). *Mammal Species of the World: A Taxonomic and Geographic Reference*, 3rd ed, edited by D. E. Wilson & D. M. Reeder, pp. 312–529. Baltimore: The Johns Hopkins University Press.

Speer, S. D., Li, Z., Buta, S., Payelle-Brogard, B., Qian, L., Vigant, F., Rubino, E., Gardner, T. J., Wedeking, T., Hermann, M., Duehr, J., Sanal, O., Tezcan, I., Mansouri, N., Tabarsi, P., Mansouri, D., Francois-Newton, V., Daussy, C. F., Rodriguez, M. R., Lenschow, D. J., Freiberg, A. N., Tortorella, D., Piehler, J., Lee, B., García-Sastre, A., Pellegrini, S. & Bogunovic, D. (2016). *Nature Commun.* **7**, 11496.

Sridharan, H., Zhao, C. & Krug, R. M. (2010). *J. Biol. Chem.* **285**, 7852–7856.

Subudhi, S., Rapin, N., Bollinger, T. K., Hill, J. E., Donaldson, M. E., Davy, C. M., Warnecke, L., Turner, J. M., Kyle, C. J., Willis, C. K. R. & Misra, V. (2017). *J. Gen. Virol.* **98**, 2297–2309.

Swaim, C. D., Scott, A. F., Canadeo, L. A. & Huibregtse, J. M. (2017). *Mol. Cell*, **68**, 581–590.

Tang, X. C., Zhang, J. X., Zhang, S. Y., Wang, P., Fan, X. H., Li, L. F., Li, G., Dong, B. Q., Liu, W., Cheung, C. L., Xu, K. M., Song, W. J., Vijaykrishna, D., Poon, L. L., Peiris, J. S. M., Smith, G. J., Chen, H. & Guan, Y. (2006). *J. Virol.* **80**, 7481–7490.

Versteeg, G. A., Hale, B. G., van Boheemen, S., Wolff, T., Lenschow, D. J. & García-Sastre, A. (2010). *J. Virol.* **84**, 5423–5430.

Walker, P. J., Widen, S. G., Firth, C., Blasdell, K. R., Wood, T. G., Travassos da Rosa, A. P. A., Guzman, H., Tesh, R. B. & Vasilakis, N. (2015). *Am. J. Trop. Med. Hyg.* **93**, 1041–1051.

Yuan, W. & Krug, R. M. (2001). *EMBO J.* **20**, 362–371.

Zhao, C., Sridharan, H., Chen, R., Baker, D. P., Wang, S. & Krug, R. M. (2016). *Nature Commun.* **7**, 12754.